16th World Conference on Earthquake, 16WCEE 2017
Santiago Chile, January 9th to 13th 2017
Paper N° 2917 (Abstract ID)
Registration Code: S-U1463183185

2015 Gorkha Post-Earthquake Reconnaissance of a Historic Village with Micro Unmanned Aerial Systems

Richard. L. Wood[(1)], Daniel. T. Gillins[(2)], Mohammad Ebrahim Mohammadi[(3)], Farid Javadnejad[(4)], Hoda Tahami[(5)], Matthew N. Gillins[(6)], and Yijun Liao[(7)]

[(1)] *Assistant Professor, Department of Civil Engr., University of Nebraska-Lincoln, Lincoln NE, USA, rwood@unl.edu*
[(2)] *Courtesy Professor, School of Civil & Construction Engr., Oregon State University, Corvallis, OR, USA, dan.gillins@oregonstate.edu*
[(3)] *Graduate Student, Department of Civil Engr., University of Nebraska-Lincoln, Lincoln NE, USA, mmohammadi2@unl.edu*
[(4)] *Graduate Student, School of Civil & Construction Engr., Oregon State University, Corvallis, OR, USA, javadnef@oregonstate.edu*
[(5)] *Graduate Student, School of Civil & Construction Engr., Oregon State University, Corvallis, OR, USA, tahamih@oregonstate.edu*
[(6)] *Graduate Student, School of Civil & Construction Engr., Oregon State University, Corvallis, OR, USA, gillinsm@oregonstate.edu*
[(7)] *Graduate Student, Department of Civil Engr., University of Nebraska-Lincoln, Lincoln NE, USA, yijun.liao419@huskers.unl.edu*

Abstract

The M7.8 Gorkha earthquake that occurred in Nepal in April 2015 and its resulting aftershocks caused extensive widespread damage to numerous built-up urban centers. One example is Bungamati, a small village approximately 12 kilometers south of Kathmandu, Nepal, that overlooks the Bagmati River. This village dates back to the 6th century and contains the Temple of Macchindranath within its city limits. Within this village, numerous, tightly-spaced masonry and earthen style structures exists in a non-grid pattern with many streets only passable by pedestrian traffic. Such a village presents significant challenges for efficient damage assessment following an extreme event, where both narrow streets and urban canyons limit vehicular access for equipment and the clear sky required to collect global navigation satellite system (GNSS) data.

In the aftermath of the earthquake series, two unmanned aerial system (UAS) platforms characterized the structural damage experienced by the village. A lightweight digital camera mounted on each platform collected visual images and both platforms flew on semi-autonomous paths. The applications of these UAS platforms permit damage assessment at a detailed level that is not achievable through satellite imagery, which has significantly less physical image resolution and at times has occlusions due to inclement weather. With these two platforms, 1300 high-definition, digital images were used to reconstruct the village into a 3D model via structure-from-motion, a computer vision technique. The resulting 3D point cloud and imagery allows for digital assessment of the structural performance. These remotely generated damage assessments were completed in a time-efficient, cost-effective, and safe manner with limited exposure to the damaged village.

Keywords: Unmanned Aerial Systems; Structure–from-Motion; Damage Detection; 2015 Gorkha Earthquake; Remote Sensing Assessment.

1 Introduction

Rapid damage assessment in the aftermath of large earthquakes is critical in terms of risk management, recovery operations, and forensic investigations of infrastructure. Critical damage scenes can be lost during recovery and cleanup operations or chaotic activities after the event. In addition, lack of data due to accessibility and communications limitations can result in delays of recovery, rescue, and rebuilding operations. In recent years, advances in satellite imaging, aerial imaging, and laser scanning show potential to perform reconnaissance and damage assessments in an objective manner [1, 2].

However, some of these methods may not be ideal for rapid damage assessment. Examples include obscured or low-resolution satellite imagery because of clouds or other environmental conditions, as well as ground-based laser scanning that requires local site access and ground support. One upcoming platform is the unmanned aerial system (UAS). UASs require only minimal ground support and site accessibility, making them an attractive platform for rapidly collecting perishable data after an extreme event. The main objective of this paper is to investigate the applicability of UAS for post-earthquake damage assessment. To accomplish this objective, aerial imagery from UASs was collected of Bungamati, a historic village that was badly damaged after the 2015 Gorkha earthquake in Nepal.

1.1 Overview of the 2015 Gorkha earthquake

The M_w 7.8 Gorkha earthquake occurred on Saturday, April 25, 2015, at 11:41 A.M. local time in the Gorkha district of central Nepal (28.15° N, 84.70° E) at a depth of 15 km. Ground shaking was felt throughout Nepal as well as regions of India, Bhutan, Bangladesh, Tibet, and China (refer to Fig. 1). Within a few days of the main seismic event, significant aftershocks of M_w 6.6 and 6.7 occurred, as well as one particularly strong aftershock of M_w 7.4 on May 12, 2015, located approximately 80 km northeast of Kathmandu [3].

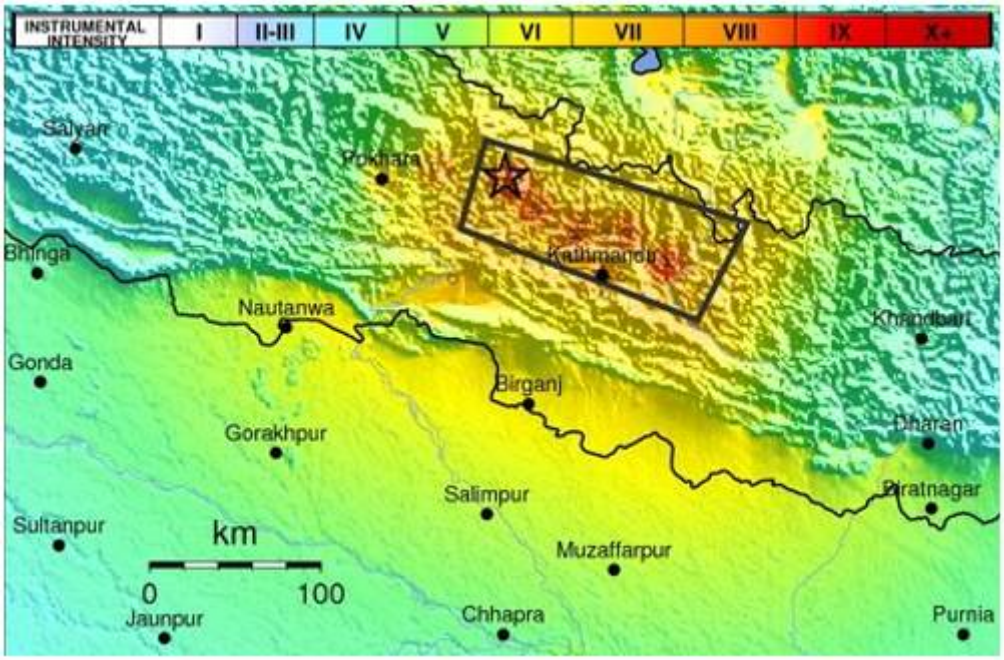

Fig. 1 - Isoseismic map of estimated Modified Mercalli Intensity scale (I-X) for the 2015 Gorkha Earthquake [4].

The Himalayan Mountains are located at the interface of two continental plates, namely the Indian and Eurasia plates. The Indian plate moves northward underneath the Eurasian plate and contributes to the seismicity of Nepal and the surrounding region [5]. The 2015 Gorkha earthquake is the most severe earthquake in this region since the 1934 Nepal-Bihar earthquake [6]. This earthquake led to widespread damage and loss of life throughout the country. In this event, an estimated number of deaths and injuries was nearly 8,600 and 22,000,

respectively. In addition, nearly 780,000 buildings were severely damaged and approximately 303,000 buildings were partially damaged [7]. Estimates of total rebuilding cost are more than $10 billion USD, which equates to 50 percent of the Nepali GDP [8].

1.2 Overview of the study area: Bungamati, Nepal

One of the regions severely affected by this earthquake event included the small village of Bungamati, located 12 km southwest of downtown Kathmandu, overlooking the Bagmati River. The village has an estimated population of 5,720 (in 2011), dates back to the 6th century, and contained the historic temple of Machhindranath, a shikhara-style temple that completely collapsed during the 2015 earthquake. This Newari village is of cultural importance to locals due to its birthplace of Rato Machhindranath. On June 27 and 29, 2015, the authors visited the village of Bungamati to conduct rapid damage assessment as well as characterize and document the structural damage. The majority of buildings in the village were constructed of masonry or earthen-style structures, made of brick and mud without any reinforcement (unreinforced masonry), and timber floor systems (flexible diaphragms) (Fig. 2). These structural systems provided little to no resistance to earthquake loads despite their significant weight resulting in widespread damage throughout the village, including numerous collapsed buildings. Surveying damage in this village was quite challenging due the non-grid and dense construction of its buildings within narrow nonlinear streets and narrow alleyways that are only passable by foot traffic. Such conditions introduce considerable challenges for an effective and efficient ground-based post-disaster assessment.

(a) (b) (c)

Fig. 2 – Overview of post-earthquake damage observed in Bungamati: (a) widespread damage to unreinforced masonry structures, (b) complete collapse of an example masonry structure, and (c) example flexible timber-diaphragm floor system.

1.3 Scope of the paper

To overcome these challenges, the team deployed two unmanned aerial system (UAS) platforms with lightweight mounted cameras to capture aerial images for damage assessment of the entire village as well as one ground-based lidar (light detection and ranging) scanner to collect data of the village. Lidar scanning, at select locations, permitted a baseline comparison of the collected UAS collected data. The objectives of this paper are to explain the methodology for UAS deployment, summarize the processing procedure of the aerial imagery, compare the accuracy of collected data against lidar (ground truth), and highlight how the results can be used for post-disaster structural assessment. Both UAS platforms were flown semi-autonomously to capture 1300 high-definition digital images. These images enabled reconstruction of a detailed three-dimensional point cloud model of the village via Structure-from-Motion (SfM) algorithms. The resulting point cloud model allows digital assessment of the damaged structures as well as preserves the significantly damaged state of the village.

This method not only provides a rapid and safe solution for damage assessment under a potential aftershock, but also introduces a cost-effective and versatile platform compared to ground-based lidar scanning.

2 Previous Reconnaissance Work via UAS and Lidar

Structural assessment using remote sensing techniques such as lidar or SfM are rapidly growing in popularity. These technologies have been used to collect data in a wide variety of applications from decision making in risk management purposes [9] to structural damage detection [10, 11]. Both methods utilize separate equipment technologies and workflows to create a point cloud for further processing and data interpretation.

2.1 Remote sensing using UAS

Remote sensing using UAS technology allows rapid collection of data. UAS-based remote sensing can be classified in two broad categories based on the data collection method, namely aerial laser scanning (ALS) and aerial photogrammetry. While ALS provides a high level of accuracy and is less susceptible to environmental conditions, it has a significant capital investment and requires a supporting base station at the ground level (usually within 50 km of the target site) [12]. On the contrary, aerial images can be captured via a camera mounted on a UAS. Using SfM, a series of overlapping multi-stereo images captured at numerous locations can be used to generate 3D point clouds similar to those produced with lidar. The 3D construction relies on the extraction of matched feature points in overlapping images of the object. SfM estimates the orientation of the camera and derives three-dimensional positions of the feature's surface by simultaneous, highly redundant, iterative bundle adjustment procedures. With these known positions and features, it can recreate the scene in terms of a point cloud. Disadvantages of SfM point clouds are that they may have some non-uniform noise and they are output in an arbitrary coordinate system. The arbitrary coordinate system can accounted for by direct georeferencing techniques, or by scaling the point cloud using points with known coordinates (i.e. lidar point clouds for small-reconstructed objects [13] or via geo-referenced ground control or survey points [14]). Previously, the potential for aerial SfM point clouds from UAS was deployed in the recent post-disaster events. In the aftermath of the M_w 8.2 Iquique 2014 Chile earthquake, a team deployed a UAS platform to study the applications of the SfM point clouds in a post-earthquake geotechnical reconnaissance. In the study, the team evaluated the accuracy of SfM point clouds by comparing the recorded earth displacements in the field against the estimated displacements in the point cloud [14]. Following the 2012 Hurricane Sandy, a team conducted a post-hurricane structural assessment using SfM point clouds. This study concluded SfM point clouds could be used for global performance evaluation of the residential buildings (e.g., wall opening damage or window damage); however, their resolution was not sufficient for detailed structural damage assessments [15]. Additionally, in the aftermath of June 14, 2014, tornado outbreak in northeast Nebraska, a post-tornado damage assessment was conducted by deploying a UAS platform and lidar to document the damage [13]. In this study, a ground-based lidar point cloud served as the primary source of spatial data to scale the SfM point cloud. Combining the SfM point cloud with the ground-based lidar point cloud significantly minimized occlusions associated with ground-based laser scanning. For example, the SfM point cloud helped fill in those parts of the roof and detailed architecture that could not be viewed or measured from the ground with the laser scanner. Accuracy of this post-tornado assessment found the SfM point cloud had an error of less than 1% in comparison to lidar; however, the error was not uniform throughout the cloud.

2.2 Remote sensing using ground-based lidar

Lidar systems rapidly and accurately map the surface of the objects by emitting and analyzing reflected laser waveforms. Lidar point clouds contain sufficient accuracy that can be used effectively in deformation analyses [16], structural damage detection [10, 17], and documenting and preserving cultural heritage to study the structural responses [18]. In post-disaster reconnaissance, ground-based lidar platforms are verified as an accurate and safe method to conduct damage assessments at a safe distance from precarious or nearly collapsed structures. In the 2010 Chile and Haiti earthquakes, ground-based lidar platforms assessed residential structural damage, cracks and concrete spalling within bridge piers, and uneven ground settlements and other deformations at foundations [2, 19]. Additionally, volumetric concrete spalling analyses and crack measurements were computed using intensity color maps [2]. Nonetheless, the ground-based stationary lidar systems are limited to accessible areas (i.e., in terms of safety and permission) and environmental conditions (e.g. pedestrian or vehicle

traffic, and detailed architectural features) that can create occlusions or shadow zones in the collected data. Occlusions can potentially affect the efficiency of the data collection process.

3 Data Collection

3.1 Establishment of ground control points

SfM can be used to reconstruct 3-D models and orthomosaics from overlapping 2-D stereo images; however, the outputs will be in an arbitrary coordinate system unless one uses direct georeferencing methods or establishes ground control points (GCPs). Direct georeferencing typically requires accurate GNSS-aided inertial navigation system (INS) data with calibrated cameras. Most inexpensive small UAS equipped with consumer-grade cameras do not include such systems; therefore, GCPs are the primary georeferencing technique used today.

Four aerial targets (similar to those in Fig. 3a) were temporarily placed in the village as GCPs. The positions of these targets were determined using two Leica GS14 GNSS receivers. One receiver was setup as the "Base" receiver that logged static GNSS data at a 15-second epoch rate for 4 hours and 20 minutes—the duration of the UAS survey campaign in Bungamati. The second receiver, the "Rover", collected 10 minutes of static GNSS data on each aerial target (Fig. 3b). Five additional points with coordinates derived from ground-based lidar were used as GCPs since it was later found that the four aerial targets were insufficient due to the village size.

(a) (b)

Fig. 3 - Demonstration of surveying technique: (a) an aerial target established in the study area, (b) GNSS rover station on an aerial target.

Raw GNSS data collected at the base receiver was submitted to Trimble CenterPoint™ RTX™ post-processing service. This web-based service uses precise point positioning (PPP) algorithms to provide geodetic coordinates at centimeter-level accuracy for GNSS observations of at least 1 hour in duration. This Trimble PPP tool performs the calculations in the ITRF-2008 reference system at the time of the GNSS observation (in this case Epoch 2015.5). Use of PPP for this project was particularly advantageous, as it did not require relative positioning against continuously operating GNSS reference stations near the project area in Nepal that may be unreliable due to the tectonic movement associated with the earthquake. Resulting coordinates from Trimble at the base were held as the control for the GNSS survey.

The geodetic coordinates of the ground control points (GCPs) were then estimated by holding the coordinates at the base fixed and by using the GNSS post processing kinematic (PPK) survey technique. PPK is a relative positioning technique that reduces errors by baseline processing of data collected from at least two GNSS receivers that are simultaneously logging observables for a minimum of four common satellites. For best results, it is recommended that the base and rover are less than 6 km apart, which was the case for this field survey. Baseline processing between the base and multiple rover positions was performed in Leica Geo Office® 8.3. Note that longest baseline from the base to a target was only 210 meters. Holding the base coordinates fixed, each of the GNSS-derived GCPs were estimated to have a 3D RMSE of 0.004 m.

3.2 UAS operations and pre-processing

Two small UAS platforms were used in this study. Both systems deploy autopilot control systems equipped with a GPS-aided Inertial Navigation System (INS). The autopilot system repeatedly interprets the aircraft orientation, position, velocity, altitude and other flight information and uses the data to stabilize the multi-rotor and perform flight commands. The aircraft receives commands through radio signals from a ground station operator, or the commands can be stored as a predefined flight mission via its on-board computer. It is possible to plan fully automated photogrammetric missions by integrating UAS autopilot capabilities with photogrammetric principals.

One system was a DJI F550 hexacopter (larger platform shown in Fig. 4a) equipped with the Wookong-M autopilot controller. The platform carried a Sony α5000 camera, which has a near-asymmetric 16-50 mm, *f*/3.5-22 lens, and a 23.5×15.6 mm size APS CMOS sensor capable of producing 5456×3632 (20 MP) pixel images. The second system was a modified DJI Phantom 2 quadcopter (smaller platform in Fig. 4a), with a Naza-M V1 autopilot system. The Phantom system was equipped with a GoPro Hero3+ Black Edition camera with a fixed 3-mm, *f*/2.8-6 lens, 1/2.3" CMOS sensor, capable of producing 4000×3000 (12 MP) pixel images. Both systems carried its camera on a stabilizing gimbal.

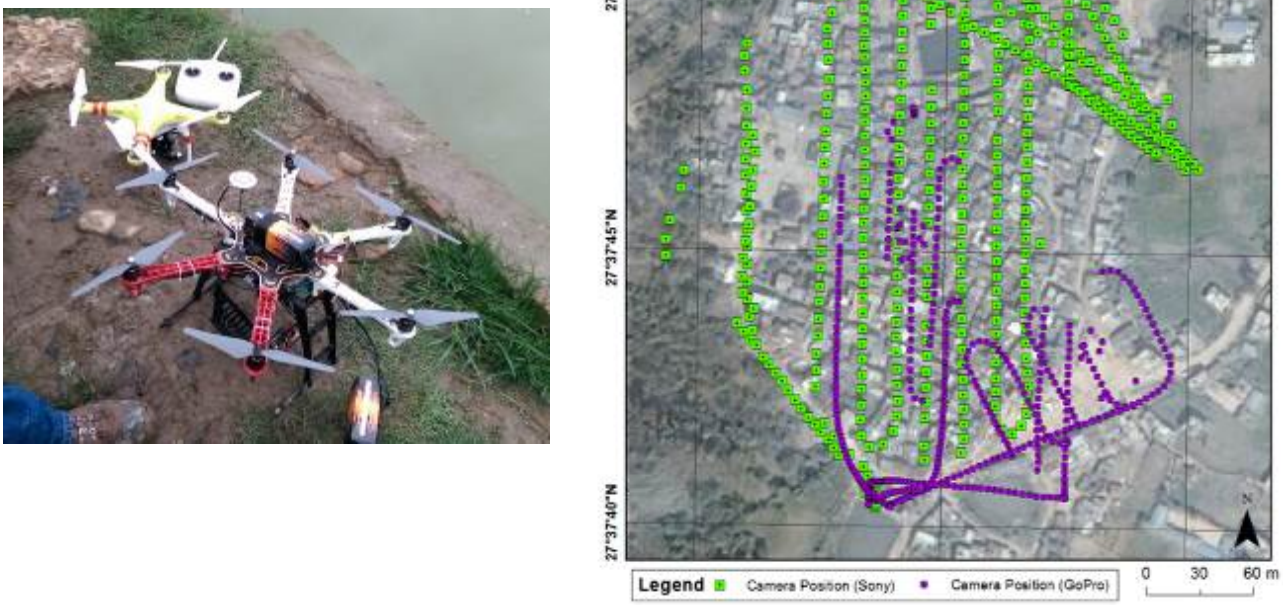

(a) (b)

Fig. 4 – (a) Remote sensing platforms: modified DJI Phantom 2 system with GoPro Hero3+ and DJI F550 system with Sony α5000 and (b) estimated camera locations on top of Esri's world imagery.

The flights were performed on June 27 and 29, 2015. DJI's software package, Ground Station®, was used for photogrammetric flight mission planning. The DJI F550 flights were performed at an altitude of 65 m (resulting in a ground-sampling distance roughly equal to 1.5 cm), with a planned side overlap of 75% (Fig. 4b). The camera shuttered in automatic focus and automatic exposure modes at one second intervals, yielding 80% forward overlap at a forward flight speed of 7 m/s. More than 700 aerial images of the roughly 1.6 km^2 village were collected during a total of 30 minutes of flight. Fig. 5a is an example of an aerial image taken from the

F550. The imagery from DJI Phantom 2 were used as complimentary dataset to F550 data. Fig. 5b shows an example of aerial images taken with wide-angle GoPro image on Phantom system.

(a) (b)

Fig. 5 - Example aerial imagery: (a) Sony α5000 and (b) example of aerial imagery from GoPro Hero3+.

The GoPro HERO 3+ Black Edition camera contains a fisheye or wide-angle lens. While the fisheye lens captures extremely wide angles of view, (i.e., 14 mm in a 35 mm equivalent system) it produces extreme image distortion (Fig. 6a). Image distortion is a significant problem in many computer vision processes, especially within SfM algorithms that can create additional undesired noise. Image distortion can be classified in to three broad categories: barrel or radial distortion, pincushion or decentering distortion, and complex distortion [20, 21]. Within a fisheye lens, the distortion is primarily barrel; however, within the optics of a GoPro camera a significant complex distortion is noted. Consequently, a MATLAB procedure was utilized to geometrically correct the images based on Brown's distortion model (Fig. 6b) [13].

(a) (b)

Fig. 6 - Example aerial image obtained from GoPro Hero 3+: (a) distorted image before correction and (b) after correction.

3.3 SfM processing

Agisoft PhotoScan® 1.1 was used for creating 3D models of the scene from the images acquired by UAS. This software is commercial photogrammetric platform for semiautomatic image-based 3D modeling. It can generate point clouds, textured polygonal models, georeferenced orthomosaics, and digital terrain models (DTMs) from overlapping 2D images. The software outputs were georeferenced by using the aforementioned GCPs.

The processing included feature detection, matching, photo alignment, dense point cloud generation, mesh building, assignment of GCPs, and orthophoto rectification. The SfM processing resulted in about 757 thousand and 530 million points in sparse and dense point clouds, respectively, and 36 million faces in the triangular irregular network (TIN) mesh. The GCPs were identified by placing a marker in the appropriate images and providing the longitude, latitude, and elevation. Putting a marker on a GCP in one image will automatically add the new marker on all images with projections of the GCP. However, separate refinement of the GCP in all

images is recommended. Ultimately, georeferencing was done by constraining the model to the coordinates of the GCPs, resulting in a point cloud fitting the GCPs by an estimated 3D RMSE of 8 cm.

Fig. 7 shows the geo-referenced point cloud for a selected region of Bungamati village, where undamaged, damaged or completely collapsed buildings can be identified. A resulting orthophoto of the area from the UAS imagery is shown in Fig. 8a. This high-resolution UAS-derived orthophoto (Fig. 8b) has a ground resolution of 2 cm. The orthophoto was overlaid and compared to satellite imagery provided by Esri. The Esri satellite imagery (Fig. 8c) is sourced to DigitalGlobe's image of Kathmandu with 0.6 m resolution and 25 m accuracy, captured on March 4, 2010 (before the earthquake). As shown in Fig. 8, the orthophoto resulted from UAS imagery has a considerably higher resolution (2 cm) compared to the existing satellite image (60 cm). The highly detailed and resolute UAS imagery is due to the low altitude maneuvering capabilities of UAS, and highlights a benefit of UAS imagery over satellite imagery.

Fig. 7 - Section of the geo-referenced 3D point cloud of Bungamati village.

In addition to the remote sensing with UAS, 33 ground-based lidar (GBL) scans were collected along the main road of Bungamati as well as in some of the more open areas in the village. The lidar scanner, Riegl Vz 400, was mounted onto a surveying tripod and transported from scan position to scan position. Due to the size of the village and ongoing recovery efforts, lidar targets were not utilized. Instead, a Leica GS14 GNSS rover antenna was fixed to the top of the scanner, and 5 minutes of static PPK GNSS data was collected at each scan position. Similar to post-processing the GNSS data on the GCPs, the baseline observations between the rover above the scanner and the base GNSS receiver were post-processed. The vertical offset between the GNSS receiver and the scanner enabled estimation of the scanner position for registration. Fig. 9 shows the Riegl Scanner with the GNSS receiver mounted on top.

Fig. 10a illustrates a map of the GNSS base station, GCPs, and lidar scan positions. Many scans of the interior sections of the village proved to be difficult to register due to the urban canyons created by the narrow alleys and multi-storied buildings. These urban canyons cause poor satellite visibility as well as short line-of-sight distances. Since this data was collected without targets, the final registration of these 33 scans was conducted in PointReg with the GNSS coordinates. PointReg requires the known coordinates of the Northing, Easting, and Height as well as the roll, pitch, and yaw. The program then iterates on the yaw and height to tighten the scan registration. This is done iteratively until the change in rotation is less than a 0.01°.

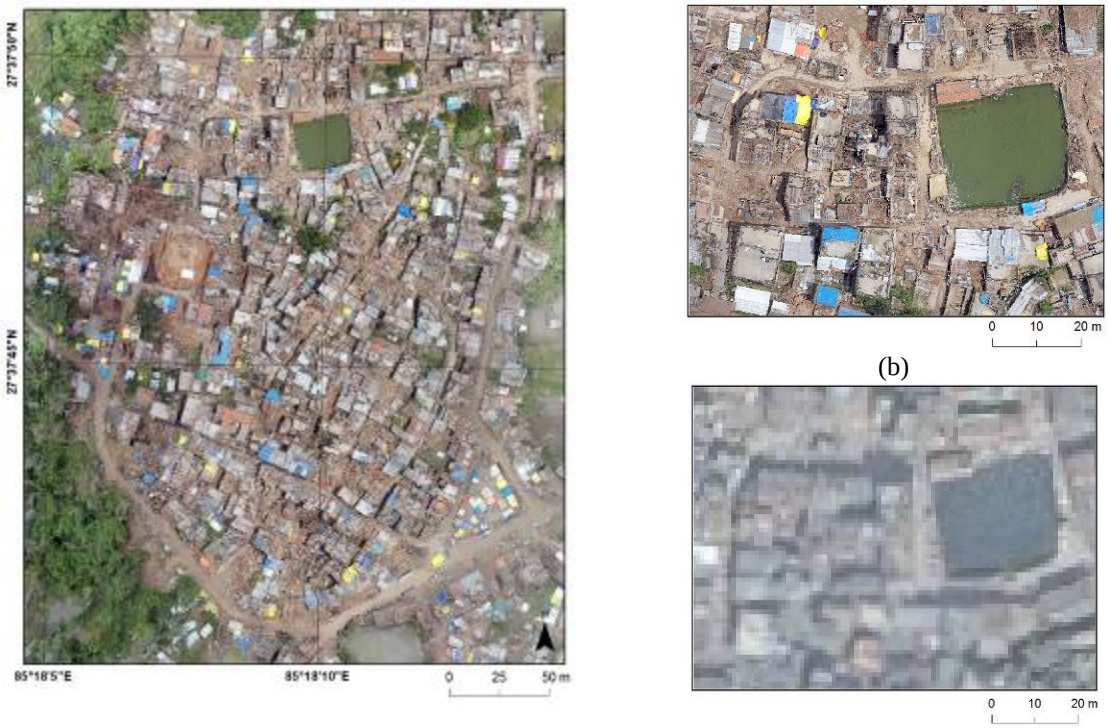

(a) (b) (c)

Fig. 8 - (a) After event: the georeferenced orthophoto with 2 cm resolution processed from UAS imagery collected on June 27, and 29, 2015, (b) a close-up view of the UAS-derived orthophoto (c) before event: satellite data from Esri's world imagery sourced to DigitalGlobe's with 0.6 m resolution, captured on March 4, 2010.

.

Fig. 9 - Riegl vz400 laser scanner with Leica GNSS GS14 on top.

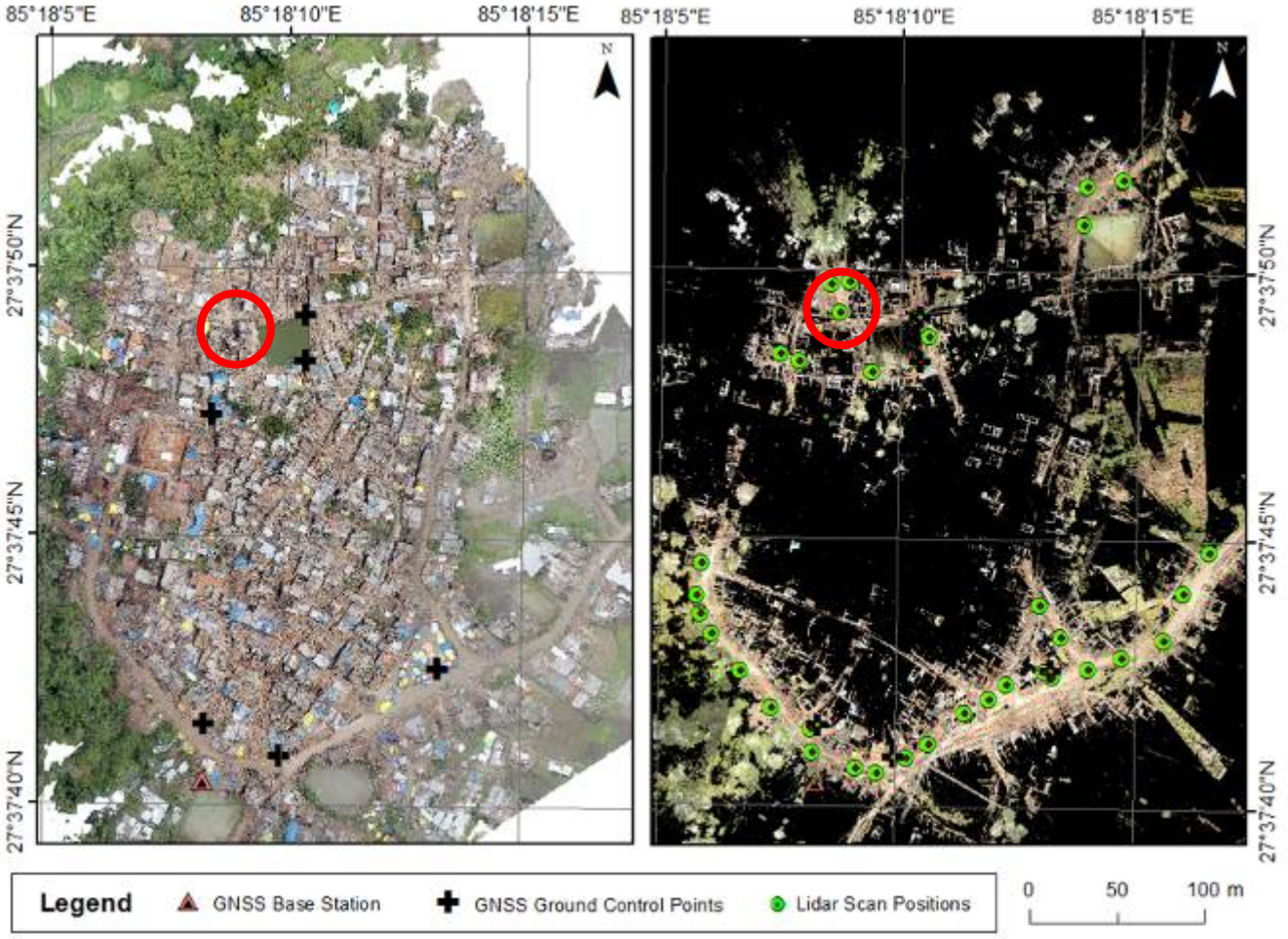

(a) (b)

Fig. 10. Map of the GNSS base station, GCPs, and lidar scan positions shown in (a) UAS-derived orthomosaic and (b) lidar scan positions and extents of the captured lidar data (black areas represent lack of data collection). Note that the red circle highlights the location of the selected site for the accuracy comparison in the next section.

4 Comparison of UAS-SfM vs. Ground-based Lidar Point Clouds

To investigate the accuracy the SfM-derived point cloud, a portion of it was compared with a ground-based lidar-derived point cloud. One building in the northwest corner of the village, as identified in Fig. 10, was extracted from both the SfM and lidar point clouds (illustrated in Fig. 11a). The exterior footprint dimensions of the building were measured for comparison. Through examination of these measurements, it is noted that the lengths vary by at most 12 centimeters, which equates to a percent difference of 1.5%. This shows a reasonably high level of accuracy within the SfM point cloud, however it is noted that the error and point density are not as uniform in the SfM point cloud as in the lidar point cloud. Nevertheless, the SfM point cloud, compared to that of lidar, has greater coverage and provides more details for the selected building at the higher elevations of the structure and supporting roof systems, which were often occluded in ground-based lidar data. Because the UAS was flying above the village, it has fewer occlusions than the ground-based lidar, and enabled much more rapid mapping of the entire village.

(a) (b) (c)

Fig. 11. Selected site for comparison: (a) top view photo (highlighted by red box), (b) SfM point cloud, and (c) lidar point cloud. Note that all measurement units are in meters.

5 Conclusions

This paper studies the applicability of UASs for rapid post-earthquake damage assessment. UASs can acquire accurate data over small to moderate areas with minimal ground support and site accessibility in a relatively short time. This paper details the post-earthquake reconnaissance of the 1.6 km^2 village of Bungamati, Nepal, with unique data sets resulting from a UAS survey as well as ground-based laser scanning survey. The collected ground-based laser scan data permitted a spot check at a selected site in the northwest corner of the village to confirm the reliability, quality, and accuracy of the UAS-collected data. This comparison highlights the potential for UAS platforms to collect reliable and spatially accurate data to create a holistic scene of an area of interest. However, detailed structural damage assessment requires more accurate and detailed data for refined assessments (at the sub-centimeter level). Another important drawback of the method is its requirement for physical scale, as limited by the deployed UAS platforms. To accomplish this task, it is necessary to establish ground control points or directly georeference the collected data to provide a real-world scale and, if desired, GNSS coordinates. Within this project, nine ground control points were used to make this coordinate transformation. Despite these limitations, the versatility, ease of deployment, accuracy of the data, and the lower ownership and operational cost of UASs make these a favorable solution for aerial mapping and post-disaster reconnaissance. Additionally, collected data is useful for decision making in recovery and rescue operations or documenting perishable damage data for forensic engineering purposes.

6 Acknowledgements

Support for this work was provided by the University of Nebraska Foundation and NSF Award #1545632 at Oregon State University. In conducting this fieldwork, the authors would like to greatly acknowledge the support from numerous individuals at Oregon State including Profs. Andre Barbosa and Michael Olsen, Mr. Patrick Burns, and Mr. Rajendra Soti; as well as Mr. Supratik Bose (University at Buffalo). Additional support and guidance for the reconnaissance efforts was provided by the National Society of Earthquake Technology (NSET) in Nepal, through the support of Ramesh Guragain and Dev Kumar Maharjan. The opinions expressed in this paper are those of the authors and do not necessarily represent those of the sponsors or the collaborators.

7 References

[1] Womble JA, Mehta K, Adams BJ (2007): Remote-sensing assessment of wind damage. 5th International Workshop on Remote Sensing Applications to Natural Hazards, Washington DC, USA.

[2] Olsen MJ, Cheung KF, YamazakI Y, Butcher S, Garlock M, Yim S, McGarity S, Robertson I, Burgos L, Young YL (2012): Damage assessment of the 2010 Chile earthquake and tsunami using terrestrial laser scanning. *Earthq. Spectra*, **28** (1), 179-197.

[3] Rai DC, Singhal V, Raj SB, Sagar SL (2015): Reconnaissance of the effects of the M7. 8 Gorkha (Nepal) earthquake of April 25, 2015. *Geomat. Nat. Haz. Risk*,**7** (1), 1-17.

[4] United State Geological Survey (2015): M7.8 – 36km E of Khudi, Nepal. http://earthquake.usgs.gov/earthquakes/eventpage/us20002926#general_region. (Feb. 19, 2016).

[5] Paudyal H, Panthi A (2010): Seismic Vulnerability in the Himalayan Region. *Himalayan Phys.*, **B** (1), 14-17.

[6] Hashash Y, Tiwari B, Moss RE, Asimaki D, Clahan KB, Kieffer DS, Dreger DS, Macdonald A, Madugo CM, Mason HB (2015): Geotechnical Field Reconnaissance: Gorkha (Nepal) Earthquake of April 25, 2015 and Related Shaking Sequence. *Geotechnical Extreme Event Reconnaissance GEER Association Report no. GEER-040*, San Luis Obispo, CA, USA.

[7] Nepal Disaster Risk Reduction Portal (2016): Incident report of earthquake 2015. http://drrportal.gov.np/, (Feb. 19, 2016).

[8] Bloomberg (2015): Nepal says earthquake rebuilding cost to exceed $10 billion. http://www.bloomberg.com/news/articles/2015-04-28/nepal-rebuilding-cost-to-exceed-10-billion-finance-chief-says, (May 13, 2016).

[9] Rehor M, Bähr H, Tarsha-Kurdi F, Landes T, Grussenmeyer P (2008): Contribution of two plane detection algorithms to recognition of intact and damaged buildings in lidar data. *Photogramm. Rec.*, **23** (124), 441-456.

[10] Mohammadi ME, Yousefianmoghadam S, Wood RL, Stavridis A (2016): Damage quantification from point clouds for finite element model calibration. *SEI/ASCE Structural Health Monitoring Applications Case Study Archive.*

[11] Torok MM, Golparvar-Fard M, Kochersberger KB (2013): Image-based automated 3D crack detection for post-disaster building assessment. *J. Comput. Civ. Eng.*, **28** (5), A4014004.

[12] Hansen J, Jonas D (1999): Airborne Laser Scanning or Aerial Photogrammetry for the Mine Surveyor. *AAM Surveys Inc.*, Brisbane, Australia.

[13] Wood RL, Mohammadi ME (2015): LiDAR scanning with supplementary UAV captured images for structural inspection. *International LiDAR Mapping Forum*, Denver, CO., USA.

[14] Rollins K, Ledezma C, Montalva G (2014): Geotechnical aspects of April 1, 2014, M8.2 Iquique, Chile earthquake. *Geotechnical Extreme Event Reconnaissance GEER Association Report no. GEER-038*, San Luis Obispo, CA, USA.

[15] Zhou Z, Gong J, Guo M (2015): Image-Based 3D Reconstruction for Posthurricane Residential Building Damage Assessment. *J. Comput. Civ. Eng.*, 04015015-1.

[16] Kayen R, Olsen MJ (2012): Post-earthquake and tsunami 3D laser scanning forensic investigations. *J. Forensic Eng.*, 2012: pp.477-486.

[17] Bose S, Nozari A, Mohammadi ME, Stavridis A, Moaveni B, Wood RL, Gillins D, Barbosa A (2016): Structural assessment of a school building in Sankhu, Nepal damaged due to torsional response during the 2015 Gorkha earthquake. *IMAC XXXIV A Conference and Exposition on Structural Dynamics*, Orlando, FL, USA, 25-28.

[18] Wittich CE, Hutchinson TC, Wood RL, Seracini M, Kuester F (2015): Characterization of Full-Scale, Human-Form, Culturally Important Statues: Case Study. *J. Comput. Civ. Eng.*, 05015001.

[19] Mosalam KM, Takhirov SM, Park, S (2014): Applications of laser scanning to structures in laboratory tests and field surveys. *Struct. Control Hlth.*, **21** (1), 115-134.

[20] Wang A, Qiu T, Shao L (2009): A simple method of radial distortion correction with center of distortion estimation. *J. Math Imaging Vis.*, **35** (3), 165-172.

[21] Zhang Z (2000): A flexible new technique for camera calibration. *IEEE T. Pattern Anal.*, **22** (11), 1330-1334.